

fast high-fidelity geometric gates for singlet-triplet qubits

Mei-Ya Chen,¹ Chengxian Zhang,^{2,*} and Zheng-Yuan Xue^{1,3,†}

¹*Guangdong Provincial Key Laboratory of Quantum Engineering and Quantum Materials, and School of Physics and Telecommunication Engineering, South China Normal University, Guangzhou 510006, China*

²*School of Physical Science and Technology, Guangxi University, Nanning 530004, China*

³*Guangdong-Hong Kong Joint Laboratory of Quantum Matter and Frontier Research Institute for Physics, South China Normal University, Guangzhou 510006, China*

(Dated: July 9, 2022)

Geometric gates that use the global property of the geometric phase is believed to be a powerful tool to realize fault-tolerant quantum computation. However, for singlet-triplet (ST) qubits in semiconductor quantum dot, the low Rabi frequency of the microwave control leads to overly long gating time, and thus the constructing geometric gate suffers more from the decoherence effect. Here, we investigate the key issue of whether the fast geometric gate can be realized for ST qubits without introducing an extra microwave-driven pulse, while maintain the high-fidelity gate operation at the same time. We surprisingly find that, both the single- and two-qubit geometric gates can be implemented via only modulating the time-dependent exchange interaction of the Hamiltonian, which can typically be on the order of \sim GHz, and thus the corresponding gate-time is of several nanoseconds. Furthermore, the obtained geometric gates are superior to their counterparts, i.e., the conventional dynamical gates for ST qubits, with a relatively high fidelity surpassing 99%. Therefore, our scheme is particularly applied to ST qubits to obtain fast and high-fidelity geometric gates. Our scheme can be also extended to other system without microwave drive.

I. INTRODUCTION

Spin qubits in semiconductor quantum dots are promising to realize universal quantum computation due to the potential scalability via combining the quantum technologies with the state-of-the-art semiconductor industry [1]. Currently, fast and high-fidelity control is still crucial for spin qubits to realize fault-tolerant quantum task. Thus, various types of qubits using the electron spin degree of freedom in the quantum dot system have been tested over the past years, including the single-dot spin qubits [2–5], double-dot singlet-triplet (ST) qubits [6–11], as well as the hybrid qubits [12, 13], triple-dot exchange-only qubits [14, 15] and resonant qubits [16, 17].

Among these possible candidates, ST qubits are particularly standing out, since it can implement all-electrical gate operation control with long coherence time and fast gate operation. Gate operation for ST qubits is implemented via tuning the Heisenberg exchange interaction between the two spins with the gate-time on the order of nanosecond thanks to the large exchange interaction (\sim GHz) [6]. Recently, researchers have experimentally observed that the relaxation time of the spin states in a quantum dot can be as long as 9 s [18], by using the isotopic purification technique in the silicon platform. Nevertheless, ST qubit in a quantum dot setup is still sensitive to the background charge noise, which occurs in the vicinity of the quantum dot [19, 20]. This hinders high-fidelity operation for either single or two-qubit quantum gates. Much works have been proposed to mitigate the charge noise, including working near the charge noise sweet spots [21], designing gates using dynamical corrected gates [22, 23].

Alternatively, the geometric phase [24] is believed to be

useful to combat noise effect. After a cyclic evolution in the parameter space, the quantum state can acquire an extra global phase factor, i.e., the Berry phase, under the adiabatic condition. Inspired by Berry’s idea, it is realized that the global property of the geometric phase can be a powerful tool for quantum computation [25–29]. However, the adiabatic condition hinders wide application of geometric gates owing to the overly long evolution time, which renders more decoherence. Recently, a universal set of quantum gates based on non-adiabatic geometric phase, namely the Aharonov-Anandan phase [30], have been realized in superconducting qubits [31–41], trapped ions [42–44], semiconductor quantum dot [45–48], etc. The core of constructing a geometric gate is to cancel out the accompanied dynamical phase during the cyclic evolution, leaving only the wanted geometric phase. Typically, this can be realized by introducing microwave field to operate its time-dependent phase to ensure the quantum state evolving always along the longitude of the Bloch sphere [48, 49].

On the other hand, the Rabi frequency of a quantum system controlled by microwave is limited in experiments. For example, in silicon-based semiconductor quantum dot for ST qubit, the exchange Rabi frequency is only several MHz [50], which is comparable to the typical values using the EDSR technology in similar devices for single-dot spin qubits [51]. Therefore, the gate-time of the desired geometric gate can be typically on the order of μ s, which is much longer than the traditional dynamical gate without using the microwave field. To fully employ the advantage of geometric gates, one has to seek ways to enable fast and appropriate operation. A good compromise is to use the Landau-Zener interferometry [52–54] with respect to the quantum state to fulfill cyclic evolution using the DC-gating pulse. However, a recent experiment [54] indicates that the dynamical phase is hard to be removed and more complicated technique like spin-echo is needed, making it impractical for quantum computation.

Here, we propose a framework to realize both single- and

*Electronic address: cxzhang@gxu.edu.cn

†Electronic address: zyxue83@163.com

two-qubit non-adiabatic geometric gates without the external microwave field, so that the gate-time can be only several nanoseconds. By only modulating the time-dependent exchange interaction, the quantum state in the parameter space can evolve along the specific geodesic line where no dynamical phase will be introduced. Thus, our method is simple but experimentally feasible. By numerically performing randomized benchmarking (RB) [55–57] and calculating the filter function [58–60] under the realistic $1/f$ noise environment, we surprisingly find that all gate-fidelities can be higher than 99%, which surpasses the conventional dynamical gate. Our results indicate that ST qubits might benefit from the preserve of the geometric operation to obtain high-fidelity control. We emphasize that our method is not only suited to the exchange-coupled ST spin qubits, but also can be readily extended to other systems that can be described by the Ising-type interacted Hamiltonian [61], such as the superconducting transmon qubits [62] and the capacitively-coupled charge qubits [63].

II. MODEL

The control Hamiltonian for a ST qubit is [22]

$$H_{\text{ST}}(t) = \frac{\hbar}{2}\sigma_x + \frac{J[\epsilon(t)]}{2}\sigma_z, \quad (1)$$

where σ_x and σ_z are Pauli matrices. The computational basic states are the spin triplet state $|0\rangle = |\text{T}(1,1)\rangle = (|\uparrow\downarrow\rangle + |\downarrow\uparrow\rangle)/\sqrt{2}$ and the singlet state $|1\rangle = |\text{S}(1,1)\rangle = (|\uparrow\downarrow\rangle - |\downarrow\uparrow\rangle)/\sqrt{2}$. Here, we define the spin state $|\downarrow\uparrow\rangle = c_{1\downarrow}^\dagger c_{2\uparrow}^\dagger |\mathcal{V}\rangle$, where $c_{i\tau}^\dagger$ ($i = 1, 2$) denotes creating an electron with spin τ at the i th quantum dot, and $|\mathcal{V}\rangle$ denotes the vacuum state. The exchange interaction $J[\epsilon(t)]$ can be controlled via operating the detuning ϵ with respect to the gate voltage, which refers to the energy splitting between the spin singlet state $|\text{S}(1,1)\rangle$ and the triplet state $|\text{T}(1,1)\rangle$. $J[\epsilon(t)]$ is with the region of $0 \leq J \leq J_{\text{max}}$. $h = g\mu\Delta B$ refers to the magnetic field gradient across the two quantum dots, where g is the electron g factor, μ is the Bohr magneton, and ΔB denotes the difference of the magnetic field between the double quantum dots. According to a recent experiment, both J and h can be obtained to be on the order of $\sim \text{GHz}$ [64], and thus the time induced from such coupling is with the order of nanosecond.

In the absence of noise, the Hamiltonian in Eq. (1) leads to the rotation with the form as

$$R(J, \phi) = e^{-\frac{i}{\hbar}\frac{\hbar\sigma_x + J\sigma_z}{2}} \frac{\phi}{\sqrt{J^2 + h^2}}, \quad (2)$$

where $R(J, \phi)$ denotes the rotation in the x - z plane by an angle ϕ , and the rotation axis in the plane is determined by J/h . In this work, we assume J as a square pulse, namely, $H_{\text{ST}}(t)$ is a piecewise Hamiltonian and therefore $R(J, \phi)$ is a one-piece rotation in a specific time duration. Hereafter, we define $U(\mathbf{r}, \phi) = \exp\left(-i\frac{\mathbf{r} \cdot \mathbf{r}}{|\mathbf{r}|^2} \frac{\phi}{2}\right)$ as rotation around an axis defined by vector \mathbf{r} . In this way we have $R(J, \phi) = U(h\hat{x} + J\hat{z}, \phi)$. The rotation out of x - z plane can be implemented by a z rota-

tion sandwiched between two x rotations [8, 65]

$$U(\hat{r}, \xi) = U(\hat{x}, \xi_1)U(\hat{z}, \xi_2)U(\hat{x}, \xi_3). \quad (3)$$

As $h > 0$ always exists, $R(J, \phi)$ cannot implement a single z -axis rotation. But, a z -axis rotation with arbitrary rotation angle can be decomposed into a three-pieces of composite sequences (the Hadamard- x -Hadamard sequence) [22], i.e.,

$$U(\hat{z}, \xi_0) = -U(\hat{x} + \hat{z}, \pi)U(\hat{x}, \xi_0)U(\hat{x} + \hat{z}, \pi). \quad (4)$$

Then, by inserting Eq. (4) into Eq. (3), one finds

$$U(\hat{r}, \xi) = U(\hat{x}, \xi_1)U(\hat{x} + \hat{z}, \pi)U(\hat{x}, \xi_2)U(\hat{x} + \hat{z}, \pi)U(\hat{x}, \xi_3). \quad (5)$$

The rotation implemented by the pulse in Eq. (1) is sensitive to noise. There are mainly two noise sources resulting in gate error. One is the charge noise, which brings fluctuation to the detuning ($\delta\epsilon$) and further leads to the error in the exchange interaction labeled by $\delta J = g[J]\delta\epsilon$, with $g[J] \propto J$ [22]. Another is the Overhauser (nuclear spin) noise, which is a time-dependent fluctuation in the background of nuclear spin bath, adding a small term into the Hamiltonian: $h \rightarrow h + \delta h$. In silicon-based semiconductor quantum dot, the isotopic purification technique can strongly suppress the Overhauser noise [4]. Meanwhile, in silicon heterostructure, it would introduce the unwanted valley-spin coupling leading to relaxation [66, 67]. According to the latest experiment [18], the relaxation time with the state-of-the-art silicon-based platform has reached $T_1 = 9$ s. In this way, we neglect the Overhauser noise and focus on the charge noise. Considering the noise effect, below any mentioned rotation $U(\hat{r}, \xi)$ or $R(J, \phi)$ is with the error term. In the following, we call them as the naive dynamical gates. In this work, our aim is to design the geometric gate to improve the naive dynamical gates.

III. SINGLE-QUBIT GEOMETRIC GATES

Here, we introduce how to construct the geometric gate via the control Hamiltonian in Eq. (1), and the evolution time can be generally separated into three parts. The Hamiltonian in each interval should satisfy

$$\begin{aligned} H_1(t) &= \frac{\hbar}{2}\sigma_x + \frac{J_1}{2}\sigma_z, & T_A \leq t \leq T_B \\ H_2(t) &= \frac{\hbar}{2}\sigma_x + \frac{J_2}{2}\sigma_z, & T_B < t \leq T_D \\ H_3(t) &= \frac{\hbar}{2}\sigma_x + \frac{J_3}{2}\sigma_z, & T_D < t \leq T \end{aligned} \quad (6)$$

with J_i ($i = 1, 2, 3$) in each part satisfying

$$\begin{aligned} \int_{T_A}^{T_B} \sqrt{J_1^2 + h^2} dt &= \frac{\pi}{2} - \theta + 2n_1\pi, & T_A \leq t \leq T_B \\ \int_{T_B}^{T_D} \sqrt{J_2^2 + h^2} dt &= \pi, & T_B < t \leq T_D \\ \int_{T_D}^T \sqrt{J_3^2 + h^2} dt &= \frac{\pi}{2} + \theta + 2n_2\pi, & T_D < t \leq T \end{aligned} \quad (7)$$

Here, θ is the parameter determined by the chosen rotation axis, as seen below. n_i ($i = 1, 2$) depends on the values of θ

$$n_1 = \begin{cases} 1, & \theta > \pi/2 \\ 0, & \theta \leq \pi/2 \end{cases} \quad n_2 = \begin{cases} 0, & \theta \geq -\pi/2 \\ 1, & \theta < -\pi/2 \end{cases} \quad (8)$$

On the other hand, since h retains a constant value during all the gate operation processing, we take $h = 1$ as our energy unit in the remainder of this work. The exchange interaction value is therefore equivalent to the ratio J/h .

The corresponding evolution operators in each segment are

$$\begin{aligned} U_1(t, T_A) &= e^{-\frac{i}{\hbar} \int_{T_A}^t H_1(t') dt'}, & T_A \leq t \leq T_B \\ U_2(t, T_B) &= e^{-\frac{i}{\hbar} \int_{T_B}^t H_2(t') dt'}, & T_B < t \leq T_D \\ U_3(t, T_D) &= e^{-\frac{i}{\hbar} \int_{T_D}^t H_3(t') dt'}, & T_D < t \leq T \end{aligned} \quad (9)$$

Taking $J_1 = J_3$ throughout this work, the total evolution operator at the final time will be

$$\begin{aligned} U_g(T, T_A) &= U_3(T, T_D) U_2(T_D, T_B) U_1(T_B, T_A) \\ &= \begin{pmatrix} \frac{i(J_1 - J_2) \cos \theta - \sqrt{J_1^2 + 1}(J_1 J_2 + 1)}{(J_1^2 + 1)\sqrt{J_2^2 + 1}} & \frac{(J_2 - J_1)(\sqrt{J_1^2 + 1} \sin \theta + i J_1 \cos \theta)}{(J_1^2 + 1)\sqrt{J_2^2 + 1}} \\ \frac{(J_1 - J_2)(\sqrt{J_1^2 + 1} \sin \theta - i J_1 \cos \theta)}{(J_1^2 + 1)\sqrt{J_2^2 + 1}} & \frac{-i(J_1 - J_2) \cos \theta + \sqrt{J_1^2 + 1}(J_1 J_2 + 1)}{(J_1^2 + 1)\sqrt{J_2^2 + 1}} \end{pmatrix}. \end{aligned} \quad (10)$$

By setting $J_1 = 0$, $J_2 = \tan(\gamma/2)$, we can further simplify $U_g(T, T_A)$ as

$$\begin{aligned} U_g(\hat{r}, \gamma) &= \begin{pmatrix} -\cos \frac{\gamma}{2} - i \sin \frac{\gamma}{2} \cos \theta & \sin \frac{\gamma}{2} \sin \theta \\ -\sin \frac{\gamma}{2} \sin \theta & -\cos \frac{\gamma}{2} + i \sin \frac{\gamma}{2} \cos \theta \end{pmatrix} \\ &= -e^{-i \frac{\gamma}{2} (\sin \theta \sigma_y - \cos \theta \sigma_z)}. \end{aligned} \quad (11)$$

$U_g(\hat{r}, \gamma)$ represents rotation around the axis $\hat{r} = (0, \sin \theta, -\cos \theta)$ on y - z plane by an angle γ , where the rotation axis is determined by θ . Other rotations that are out of y - z plane can be implemented by using either the sequence y - z - y or z - y - z , similar to the case in Eq. 3.

To demonstrate $U_g(\hat{r}, \gamma)$ is the desired geometric gate, we introduce the orthogonal dressed states

$$\begin{aligned} |\psi_+\rangle &= \cos \frac{\theta}{2} |0\rangle - i \sin \frac{\theta}{2} |1\rangle, \\ |\psi_-\rangle &= i \sin \frac{\theta}{2} |0\rangle - \cos \frac{\theta}{2} |1\rangle. \end{aligned} \quad (12)$$

For an arbitrary operator $U_g(\hat{r}, \gamma)$ with respect to θ , its evolution can be visualized by the Bloch sphere using the dressed states, as shown in Fig. 1(a). The evolution of the dressed state $|\psi_+\rangle$ (the case for $|\psi_-\rangle$ is similar) follows the process as

$$|\psi_+\rangle \xrightarrow{U_1} |\psi_+^B\rangle \xrightarrow{U_2} |\psi_+^D\rangle \xrightarrow{U_3} e^{i(\frac{\gamma}{2} + \pi)} |\psi_+\rangle, \quad (13)$$

where

$$\begin{aligned} |\psi_+^B\rangle &= \cos \frac{\pi}{4} |0\rangle - i \sin \frac{\pi}{4} |1\rangle, \\ |\psi_+^D\rangle &= e^{i\pi} e^{i\frac{\gamma}{2}} \left(\cos \frac{\pi}{4} |0\rangle + i \sin \frac{\pi}{4} |1\rangle \right). \end{aligned} \quad (14)$$

Specifically, the dressed state starts from the given point A at the initial time T_A . Under the action of $U_1(T_B, T_A)$, it travels along the longitude denoted by A-B to point B at T_B and the state turns to be $|\psi_+^B\rangle$. Then, it evolves to $|\psi_+^D\rangle$ along the

path denoted by B-C-D due to $U_2(T_D, T_B)$. Here, the evolution path B-C-D is not along the longitude but a specific geodesic of the Bloch sphere. Finally, it goes back to the starting point A along path D-E-A owing to $U_3(T, T_D)$, where the path shares the same longitude with the one of path A-B. The overall effect of $U(T, T_A)$ is to drive the dressed state $|\psi_{\pm}\rangle$ to fulfill a cyclic evolution with the path A-B-C-D-E-A and thus obtain a corresponding global phase $\pm(\frac{\gamma}{2} + \pi)$. Therefore,

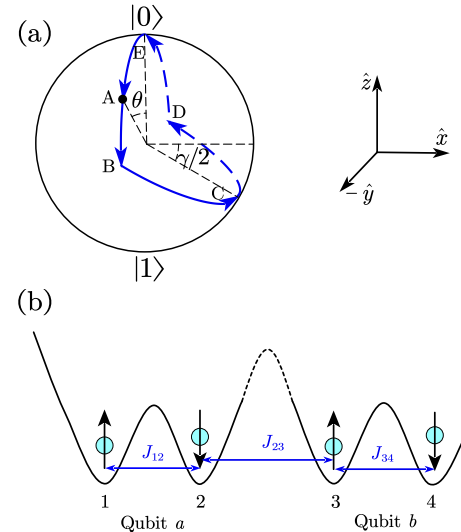


FIG. 1: (a) The schematic of the evolution path to induce a geometric gate. The dressed state $|\psi_+\rangle$ evolves along the cyclic path A-B-C-D-E-A to obtain the global geometric phase so as to get a desired geometric gate. (b) A lateral four-quantum-dot system with each dot labeled by 1, 2, 3 and 4, from the left to the right to enable two-qubit operation for ST qubits, where dot 1 and 2 form qubit a, and dot 3 and 4 form qubit b. The quantum dots are coupled via the exchange interaction denoted by $J_{i,i+1}$ ($i = 1, 2, 3$).

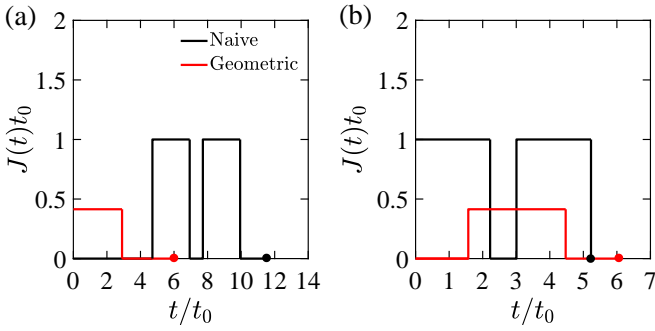


FIG. 2: The pulse shapes for the geometric gates $U_g(\hat{y}, \pi/4)$ in (a) and $U_g(\hat{z}, \pi/4)$ in (b) are compared with that of the corresponding naive dynamical gates $U(\hat{y}, \pi/4)$ and $U(\hat{z}, \pi/4)$. The black solid line denotes naive dynamical gate, while the red solid line implies the geometric gate. The time unit is determined by $t_0 = 1/h$.

$U_g(\hat{r}, \gamma)$ can also be described as:

$$U_g(\hat{r}, \gamma) = e^{i(\frac{\gamma}{2} + \pi)} |\psi_+\rangle\langle\psi_+| + e^{i(-\frac{\gamma}{2} - \pi)} |\psi_-\rangle\langle\psi_-|. \quad (15)$$

One can easily verify that for the designed evolution path in this work, the parallel transport condition [68] for geometric gate is always satisfied for each segment, i.e.,

$$\begin{aligned} \langle\psi_{\pm}|U_1^{\dagger}(t, T_A)H_1(t)U_1(t, T_A)|\psi_{\pm}\rangle &= 0, \\ \langle\psi_{\pm}^B|U_2^{\dagger}(t, T_B)H_2(t)U_2(t, T_B)|\psi_{\pm}^B\rangle &= 0, \\ \langle\psi_{\pm}^D|U_3^{\dagger}(t, T_D)H_3(t)U_3(t, T_D)|\psi_{\pm}^D\rangle &= 0. \end{aligned} \quad (16)$$

Therefore, the global phase that is obtained is the pure geometric phase, and $U_g(\hat{r}, \gamma)$ represents the pure geometric gate. It is worth mentioning that, to cancel out the dynamical phase, the conventional method [48, 49] is to evolve the dressed states always along the longitude. However, this condition is not strict here.

Next, we analyze the robustness of the geometric gates compared with the naive dynamical gates. Here, we consider two typical rotations, i.e., $U_g(\hat{y}, \pi/4)$ ($U(\hat{y}, \pi/4)$) and $U_g(\hat{z}, \pi/4)$ ($U(\hat{z}, \pi/4)$). For the geometric gate $U_g(\hat{y}, \pi/4)$ with $\theta = \pi/2$ and $\gamma = \pi/4$, the used parameters are: $J_1 = 0$, $J_2 = \tan(\pi/8)$, and the time duration with respect to each interval is $T_{AB} = 0$, $T_{BD} = \pi \cos(\pi/8)$ and $T_{DA} = \pi$. While for the corresponding naive dynamical gate $U(\hat{y}, \pi/4)$ used in Eq. (5) we have $\xi_1 = 3\pi/2$, $\xi_2 = \pi/4$ and $\xi_3 = \pi/2$. For $U_g(\hat{z}, \pi/4)$, with $\theta = \pi$, $\gamma = \pi/4$, the used parameters are: $J_1 = 0$, $J_2 = \tan(\pi/8)$, $T_{AB} = T_{DA} = 3\pi/2$ and $T_{BD} = \pi \cos(\pi/8)$. For the naive dynamical gate $U(\hat{z}, \pi/4)$ designed using the expression in Eq. (4), we have $\xi_0 = \pi/4$. The pulse shapes for the geometric and the naive dynamical gates are plotted in Fig. 2. In Fig. 3, we show their fidelities as a function of $\delta\epsilon$. Here, $\delta\epsilon$ is assumed to be a quasi-static noise and its time-dependent effect will be considered later. In all the considered region $-0.1 \leq \delta\epsilon \leq 0.1$, which implies $-0.1 \leq \delta J/J \leq 0.1$, the geometric gate can outperform its counterpart, i.e., the naive dynamical gate. We notice that for both two naive gates, when $\delta\epsilon$ becomes large the related fidelity drops quickly. Whereas, the fidelity for the geometric

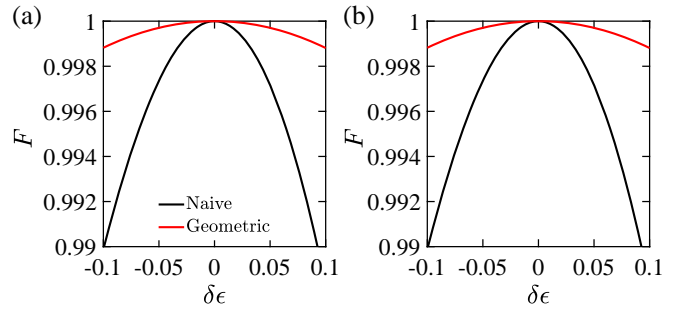


FIG. 3: The fidelity is as a function of $\delta\epsilon$, where the charge noise is $\delta J \rightarrow g[J]\delta\epsilon$. The geometric gates $U_g(\hat{y}, \pi/4)$ in (a) and $U_g(\hat{z}, \pi/4)$ in (b) are compared with the naive dynamical gates $U(\hat{y}, \pi/4)$ and $U(\hat{z}, \pi/4)$.

gates varies slowly as $\delta\epsilon$ is increasing. In addition, the advantage of the geometric gates over the naive ones becomes more and more pronounced when $\delta\epsilon$ is large.

On the other hand, the performance of the geometric gate in the real experimental noise environment in semiconductor quantum dot remains to be verified, where the noise typically varies over time. For the piecewise control Hamiltonian, the filter function [58–60] is a powerful tool to evaluate the fidelity for the time-dependent noise. The detail of the filter function is described in Appendix A, where it is defined as $F_i(\omega)$ ($i = x, z$) in the frequency domain with the noise appearing in σ_i term of the Hamiltonian. Note that, for the single-qubit case, the charge noise exists in σ_z direction. Therefore, the filter function is

$$\mathcal{F} = 1 - \frac{1}{\pi} \int_{\omega_{\text{ir}}}^{\omega_{\text{uv}}} \frac{d\omega}{\omega^2} F_z(\omega) S(\omega), \quad (17)$$

where $S(\omega)$ is the noise power spectral density in the frequency domain, ω_{uv} and ω_{ir} are the cutoff frequency. The filter functions for rotation $U_g(\hat{y}, \pi/4)$ ($U(\hat{y}, \pi/4)$) and $U_g(\hat{z}, \pi/4)$ ($U(\hat{z}, \pi/4)$) are shown in Fig. 4 (a) and (b), respectively. For both two rotations, the lines for the geometric gates are below the ones for the naive dynamical gates, which qualitatively implies the smaller infidelity for the geometric gates compared to their dynamical counterparts.

Here, we consider the $1/f^\alpha$ noise, which is the typical noise model to describe the time-dependent charge noise in semiconductor quantum dot. The power spectral density with respect to the charge noise can be written as [69]

$$S(\omega) = \frac{A_J}{(\omega t_0)^\alpha}, \quad (18)$$

where A_J is the noise amplitude, and the exponent α denotes how much the noise is correlated. $t_0 = 1/h$ is the time unit, and we take $h/(2\pi) = 1$ GHz [64]. The noise amplitude can be determined by [8]

$$\int_{\omega_{\text{ir}}}^{\omega_{\text{uv}}} \frac{A_J}{(\omega t_0)^\alpha} d\omega = \pi \left(\frac{\sigma_J}{J t_0} \right)^2, \quad (19)$$

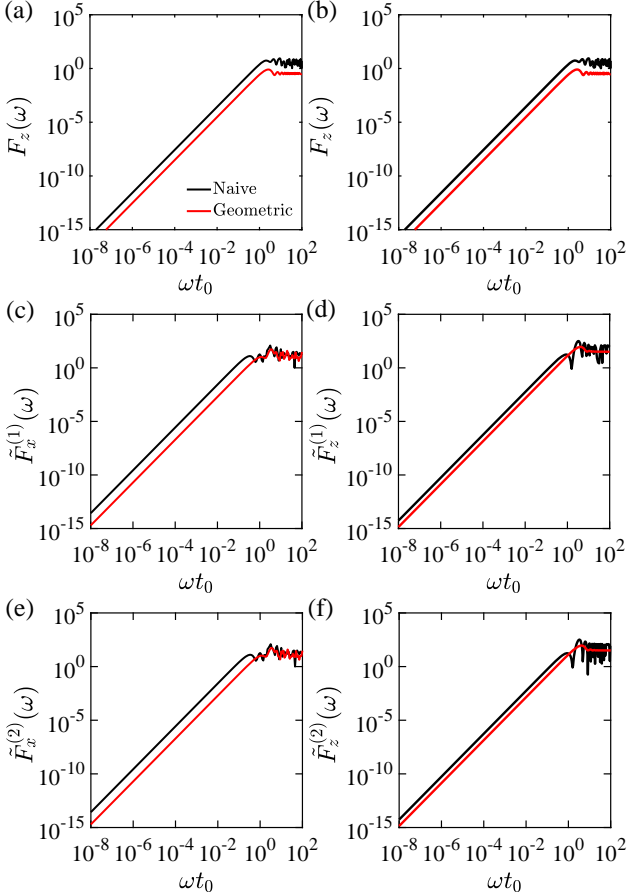


FIG. 4: The filter function in panel (a) and (b) are responsible for $U_g(\hat{y}, \pi/4)$ ($U(\hat{y}, \pi/4)$) and $U_g(\hat{z}, \pi/4)$ ($U(\hat{z}, \pi/4)$), respectively. For the single-qubit case, we only consider the z -component noise which is described by $F_z(\omega)$. While the filter function for the two-qubit CZ gate is present in (c)-(f). The superscript $i = 1, 2$ denotes the i th block, and the subscript $i = x, z$ denotes the noise appearing in the effective $\tilde{\sigma}_i$ term. The used parameters are: $h/(2\pi) = 1$ GHz [64], $S(\omega) = A_J/(\omega t_0)^\alpha$ with $A_J t_0 = 10^{-4}$ and $\alpha = 1$. The cutoffs are $\omega_{\text{ir}} = 50$ kHz and $\omega_{\text{uv}} = 1$ MHz.

where σ_J represents the standard deviation for charge noise. Typically, in semiconductor quantum dot environment [70], we have $\alpha = 1$ for the charge noise and the cutoffs are $\omega_{\text{ir}} = 50$ kHz and $\omega_{\text{uv}} = 1$ MHz. In experiments, detuning can be operated via either symmetric (barrier) control or tilt control, which corresponds to $\sigma_J/J = 0.00426$ for barrier control and 0.0563 for tilt control, respectively [21]. Therefore, the noise amplitude region is about $2.0 \times 10^{-5} \leq A_J t_0 \leq 3.3 \times 10^{-3}$. In our simulation we have considered a medium value of $A_J t_0 = 10^{-4}$ if not mentioned specifically. We find that, the fidelities related to $U_g(\hat{y}, \pi/4)$ and $U(\hat{y}, \pi/4)$ are $\mathcal{F}_{\text{nai}} = 99.974\%$, $\mathcal{F}_{\text{geo}} = 99.997\%$, while for $U_g(\hat{z}, \pi/4)$ and $U(\hat{z}, \pi/4)$, the fidelities are also $\mathcal{F}_{\text{nai}} = 99.974\%$, $\mathcal{F}_{\text{geo}} = 99.997\%$.

Except for the filter function, RB [55–57] is another effective technique to provide the average error for either all the gates on the Bloch sphere or specific gate from the Clifford group. The former is related to the standard benchmark-

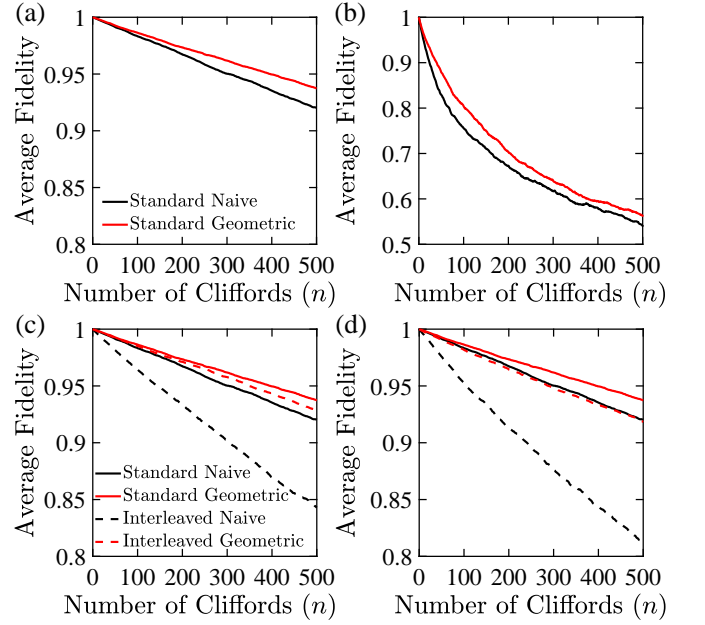


FIG. 5: RB for naive dynamical and geometric gates for $1/f^\alpha$ charge noise. The standard RB results are shown in (a) and (b), while the interleaved RB results present in (c) and (d) with respect to $U_g(\hat{y}, \pi/4)$ ($U(\hat{y}, \pi/4)$) and $U_g(\hat{z}, \pi/4)$ ($U(\hat{z}, \pi/4)$), respectively. The used parameters are: $h/(2\pi) = 1$ GHz [64], $S(\omega) = A_J/(\omega t_0)^\alpha$ with $A_J t_0 = 10^{-4}$. The noise exponent $\alpha = 1$ and 2 corresponding to the left and right column, respectively. The cutoffs are $\omega_{\text{ir}} = 50$ kHz and $\omega_{\text{uv}} = 1$ MHz.

ing, while the latter the interleaved benchmarking. The basis idea of the standard RB [22] is that for a given noise spectrum, we average the fidelity over many gate sequences which are randomly drawn from the single-qubit Clifford group composed of 24 specific gate operations, and over random noise realizations. For each run of the sequences in our simulation, the noise is attributed to the $1/f$ form as described in Eq. (18). While the interleaved benchmarking is a slight variant of the standard RB, where the specific gate to be estimated and the randomly chosen Clifford gate sequence interleave with each other [57]. To ensure convergence, we have averaged the benchmarking over 1000 times of realizations.

The standard RB results are shown in Fig. 5 (a) and (b). By fitting the resulted fidelity curve to $(1 + e^{-dn})/2$, one can obtain the average error per gate d , where n denotes the number of the used Clifford gates [69]. The corresponding average fidelity per gate is therefore $\mathcal{F} = 1 - d$. For the typical value of $\alpha = 1$ in Fig. 5 (a), the average fidelity for the naive dynamical gate and the geometric gate are $\mathcal{F}_{\text{nai}} = 99.965\%$ and $\mathcal{F}_{\text{geo}} = 99.972\%$. On the other hand, the charge noise spectrum with $\alpha = 2$ [71] has also been observed in a recent experiment. The corresponding RB result is shown in Fig. 5 (b), where the fidelity for the two types of gates are $\mathcal{F}_{\text{nai}} = 99.468\%$ and $\mathcal{F}_{\text{geo}} = 99.565\%$. With the standard RB results in mind, one can further calculate the interleaved RB fidelity [57] as $\mathcal{F}_{\text{in}} = 1 - (1 - p_{\text{in}}/p_{\text{st}})/2$, where p_{st} and p_{in} are the depolarizing parameters for the standard RB and the interleaved RB, respectively, which are deter-

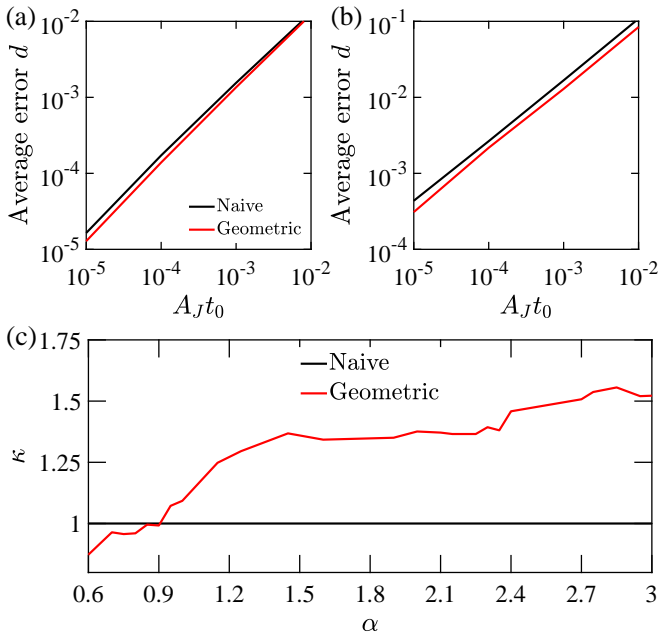


FIG. 6: Average error per gate d vs charge noise amplitude A_Jt_0 for $1/f^\alpha$ noise, where the noise exponent $\alpha = 1$ in (a) and 2 in (b). (c) Improvement ratio κ vs α .

mined by $p = e^{-d}$. The interleaved RB results for the gates $U_g(\hat{y}, \pi/4)$ and $U(\hat{y}, \pi/4)$ in Fig. 5 (c) are $\mathcal{F}_{\text{nai}} = 99.980\%$ and $\mathcal{F}_{\text{geo}} = 99.998\%$. While for the gates $U_g(\hat{z}, \pi/4)$ and $U(\hat{z}, \pi/4)$ in Fig. 5 (d), the results are $\mathcal{F}_{\text{nai}} = 99.970\%$ and $\mathcal{F}_{\text{geo}} = 99.995\%$.

To fully reveal the superiority of the geometric gate, we fur-

ther consider its performance compared to the naive dynamical one for a wide range of α and noise amplitude A_J . In Fig. 6 (a) and (b) we show the standard average error per gate d as a function of the noise amplitude A_Jt_0 considering the α values related to the recent experiment [71]. For $\alpha = 1$ in Fig. 6 (a), when A_Jt_0 is small, the two lines for the naive and geometric gates are almost parallel (the related experimental noise amplitude A_Jt_0 is from 10^{-5} to 10^{-3}). However, when A_Jt_0 is large enough (surpassing 10^{-3}), these two lines are increasingly overlapping which means there is no improvement for the naive dynamical gates. For $\alpha = 2$ in Fig. 6 (b), the line standing for the geometric gate is lower than the one for the naive dynamical gates in the whole considered noise amplitude. This means the geometric gate is more powerful for large α . In Fig. 6 (c), We further introduce an improvement ratio κ , which is defined as the error of the naive dynamical gates divided by that of the geometric ones in the small noise amplitude region. We can see that this improvement ratio κ is increasing as α becomes large. When $\alpha \leq 0.9$, κ is less than one, which means the geometric gate performs worse. For the typical noise exponent $\alpha = 1$, we have $\kappa = 1.1$. While for the case $\alpha = 2.85$, the improvement ratio is 1.56.

IV. TWO-QUBIT GEOMETRIC GATES

The Hamiltonian of the exchange-coupled two ST qubits, as shown in Fig. 1(b), is in a Ising-like form [72], namely, the qubits are coupled via the form of $\sigma_z \otimes \sigma_z$ interaction. This model is also applied for the capacitively-coupled charge qubits in semiconductor quantum dot [63], the superconducting transmon qubits operated in the dispersive regime [62], and also the NMR system [73]. For our case, the two-qubit Hamiltonian for the two double-dot system is [66, 74]

$$H_{d0} = \frac{J_{12}}{2} \tilde{\sigma}_a^x \otimes \tilde{I}_b + \frac{J_{34}}{2} \tilde{I}_a \otimes \tilde{\sigma}_b^x - \frac{J_{23}}{4} \tilde{\sigma}_a^z \otimes \tilde{\sigma}_b^z + h_a \tilde{\sigma}_a^z \otimes \tilde{I}_b + h_b \tilde{I}_a \otimes \tilde{\sigma}_b^z \\ = \begin{pmatrix} -J_{23}/4 + h_b + h_a & J_{34}/2 & J_{12}/2 & 0 \\ J_{34}/2 & J_{23}/4 - h_b + h_a & 0 & J_{12}/2 \\ J_{12}/2 & 0 & J_{23}/4 + h_b - h_a & J_{34}/2 \\ 0 & J_{12}/2 & J_{34}/2 & -J_{23}/4 - h_b - h_a \end{pmatrix}. \quad (20)$$

For convenience, here we have redefined the basis states as $\{|0\tilde{0}\rangle, |\tilde{0}1\rangle, |\tilde{1}0\rangle, |\tilde{1}\tilde{1}\rangle\} = \{|\uparrow_a\downarrow_a, \uparrow_b\downarrow_b\rangle, |\uparrow_a\downarrow_a, \downarrow_b\uparrow_b\rangle, |\downarrow_a\uparrow_a, \uparrow_b\downarrow_b\rangle, |\downarrow_a\uparrow_a, \downarrow_b\uparrow_b\rangle\}$. In the following, we use this basis state to describe the two-qubit operation. The Pauli matrices are thus slightly different as before

$$\begin{aligned} \tilde{\sigma}_i^x &= |\uparrow\downarrow\rangle_i \langle \downarrow\uparrow|_i + |\downarrow\uparrow\rangle_i \langle \uparrow\downarrow|_i, \\ \tilde{\sigma}_i^z &= |\uparrow\downarrow\rangle_i \langle \uparrow\downarrow|_i - |\downarrow\uparrow\rangle_i \langle \downarrow\uparrow|_i, \\ \tilde{I}_i &= |\uparrow\downarrow\rangle_i \langle \uparrow\downarrow|_i + |\downarrow\uparrow\rangle_i \langle \downarrow\uparrow|_i. \end{aligned} \quad (21)$$

where $i = a, b$ denotes the qubit number. h_i is the gradient for each qubit. $J_{k,k+1}$ ($k = 1, 2, 3$) denotes exchange couplings between neighboring dots. Assuming $h_a, h_b \ll J_{23}$ [74] and

setting $J_{12} = 0$, H_{d0} turns to be a block-diagonal matrix

$$H_d = \begin{pmatrix} -J_{23}/4 & J_{34}/2 & 0 & 0 \\ J_{34}/2 & J_{23}/4 & 0 & 0 \\ 0 & 0 & J_{23}/4 & J_{34}/2 \\ 0 & 0 & J_{34}/2 & -J_{23}/4 \end{pmatrix}. \quad (22)$$

In this way, we can decompose H_d into two independent subsystems with each subsystem being a 2×2 matrix

$$H_{d1} = \begin{pmatrix} -J_{23}/4 & J_{34}/2 \\ J_{34}/2 & J_{23}/4 \end{pmatrix}, H_{d2} = \begin{pmatrix} J_{23}/4 & J_{34}/2 \\ J_{34}/2 & -J_{23}/4 \end{pmatrix}. \quad (23)$$

Thus, we can treat each block as the single-qubit case, and design the corresponding geometric operation as similar in section. III. For the first block H_{d1} , we aim to design a single geometric gate. Similarly to the single-qubit case in Eq. 7 the three-pieces of evolution needs to satisfy

$$\begin{aligned} \int_{T_A}^{T_B} \sqrt{\left(-\frac{J_{23}^{(1)}}{4}\right)^2 + \left(\frac{J_{34}}{2}\right)^2} dt &= \frac{\frac{\pi}{2} - \chi}{2} + 2m_1\pi, \quad T_A \leq t \leq T_B \\ \int_{T_B}^{T_D} \sqrt{\left(-\frac{J_{23}^{(2)}}{4}\right)^2 + \left(\frac{J_{34}}{2}\right)^2} dt &= \pi/2, \quad T_B < t \leq T_D \\ \int_{T_D}^T \sqrt{\left(-\frac{J_{23}^{(3)}}{4}\right)^2 + \left(\frac{J_{34}}{2}\right)^2} dt &= \frac{\frac{\pi}{2} + \chi}{2} + 2m_2\pi, \quad T_D < t \leq T \end{aligned} \quad (24)$$

While for the second block H_{d2} , the geometric gate requires

$$\begin{aligned} \int_{T_A}^{T_B} \sqrt{\left(\frac{J_{23}^{(1)}}{4}\right)^2 + \left(\frac{J_{34}}{2}\right)^2} dt &= \frac{\frac{\pi}{2} - \chi}{2} + 2m_1\pi, \quad T_A \leq t \leq T_B \\ \int_{T_B}^{T_D} \sqrt{\left(\frac{J_{23}^{(2)}}{4}\right)^2 + \left(\frac{J_{34}}{2}\right)^2} dt &= \pi/2, \quad T_B < t \leq T_D \\ \int_{T_D}^T \sqrt{\left(\frac{J_{23}^{(3)}}{4}\right)^2 + \left(\frac{J_{34}}{2}\right)^2} dt &= \frac{\frac{\pi}{2} + \chi}{2} + 2m_2\pi, \quad T_D < t \leq T \end{aligned} \quad (25)$$

where χ is similar to θ as shown in the single-qubit case, whose parameter is determined by the chosen rotation axis, as seen below. In addition, we assume $J_{23}^{(1)} = J_{23}^{(3)}$. m_i ($i = 1, 2$) depends on the values of χ

$$m_1 = \begin{cases} 1, & \chi > \pi/2 \\ 0, & \chi \leq \pi/2 \end{cases} \quad m_2 = \begin{cases} 0, & \chi \geq -\pi/2 \\ 1, & \chi < -\pi/2 \end{cases} \quad (26)$$

Here, we assume $J_{23}^{(i)}$ ($i = 1, 2, 3$) is time-dependent and the others remain unchanged. By setting $J_{23}^{(1)} = J_{23}^{(3)} = 0$ and $J_{23}^{(2)} = 2J_{34} \tan(\gamma/2)$, one can acquire a two-qubit perfect entangling gate depending on the chosen value of γ as

$$U_{\text{ent}} = \begin{pmatrix} -\cos \frac{\gamma}{2} + i \cos \chi \sin \frac{\gamma}{2} & -\sin \frac{\gamma}{2} \sin \chi & 0 & 0 \\ \sin \frac{\gamma}{2} \sin \chi & -\cos \frac{\gamma}{2} - i \cos \chi \sin \frac{\gamma}{2} & 0 & 0 \\ 0 & 0 & -\cos \frac{\gamma}{2} - i \cos \chi \sin \frac{\gamma}{2} & \sin \frac{\gamma}{2} \sin \chi \\ 0 & 0 & -\sin \frac{\gamma}{2} \sin \chi & -\cos \frac{\gamma}{2} + i \cos \chi \sin \frac{\gamma}{2} \end{pmatrix}, \quad (27)$$

where the so-called perfect entangling gate can generate the maximally entangled states, e.g., the CNOT gate [75]. Generally, whether a two-qubit gate belongs to a perfect entangling gate can be verified by calculating the local invariants with respect to the matrix of this gate. A detailed description of the local invariant is given in Appendix B, where the local invariant G_i ($i = 1, 2, 3$) is defined. When taking $\gamma = \pi/2$, we calculate the local invariants of U_{ent} : $G_1 = G_2 = 0, G_3 = 1$, which satisfies the condition for the perfect perfect entangling operation [75]. It is of great interest that if we further take $\chi = 0$, U_{ent} is equivalent to a CZ gate [76]

$$U_{\text{CZ}} = e^{-i\frac{\gamma}{2}} \begin{pmatrix} 1 & 0 & 0 & 0 \\ 0 & e^{i\gamma} & 0 & 0 \\ 0 & 0 & e^{i\gamma} & 0 \\ 0 & 0 & 0 & 1 \end{pmatrix}. \quad (28)$$

The control Hamiltonian in Eq. (22) can alternatively implement a dynamical two-qubit gate, where the method is similar to the case in section. II. For the first block, arbitrary rotation can be obtained via a composite pulse sequence like Eq. 5

$$\begin{aligned} U_{d1}(\hat{r}, \eta) &= U(\hat{x}, \eta_1)U(-\hat{z} + \hat{x}, \pi)U(\hat{x}, \eta_2) \\ &\quad U(-\hat{z} + \hat{x}, \pi)U(\hat{x}, \eta_3), \end{aligned} \quad (29)$$

while for the second block

$$\begin{aligned} U_{d2}(\hat{r}, \eta) &= U(\hat{x}, \eta_1)U(\hat{z} + \hat{x}, \pi)U(\hat{x}, \eta_2) \\ &\quad U(\hat{z} + \hat{x}, \pi)U(\hat{x}, \eta_3). \end{aligned} \quad (30)$$

To acquire the dynamical perfect entangling gate U_{ent} , we set $\eta_1 = \pi + \chi, \eta_2 = \gamma$ and $\eta_3 = \pi - \chi$.

Normally, it is difficult to perform two-qubit RB simulation, since there are more than 10000 elements in the two-qubit Clifford group. In this way, we consider calculating the fidelity of U_{ent} via the filter function, as similar for the single-qubit case. The charge noise leads to the error in both the effective $\tilde{\sigma}_z$ and $\tilde{\sigma}_x$ terms of the Hamiltonian for each block: $\delta J_{23} \propto J_{23}$ and $\delta J_{34} \propto J_{34}$. For simplicity, here we assume these two noise sources are independent with each other. For each block, the fidelity is

$$\mathcal{F}^{(i)} \simeq 1 - \frac{1}{\pi} \int_{\omega_{\text{ir}}}^{\omega_{\text{uv}}} \frac{d\omega}{\omega^2} [S(\omega) \tilde{F}_x^{(i)}(\omega) + S(\omega) \tilde{F}_z^{(i)}(\omega)], \quad (31)$$

where $\mathcal{F}^{(i)}$ ($i = 1, 2$) denotes the fidelity for the i th block, while $\tilde{F}_x^{(i)}$ and $\tilde{F}_z^{(i)}$ represent the \tilde{x} and \tilde{z} -component filter function for corresponding block. The filter function results are shown in Fig. 4 (c)-(f). We find the geometric lines are un-

χ	$\mathcal{F}_{\text{nai}}^{(1)}$	$\mathcal{F}_{\text{geo}}^{(1)}$	$\mathcal{F}_{\text{nai}}^{(2)}$	$\mathcal{F}_{\text{geo}}^{(2)}$	\mathcal{F}_{nai}	\mathcal{F}_{geo}
$-\pi/2$	98.538%	99.692%	98.538%	99.692%	97.678%	99.508%
$-\pi/4$	98.525%	99.688%	98.525%	99.688%	97.658%	99.503%
0	98.509%	99.685%	98.509%	99.685%	97.633%	99.496%
$\pi/4$	98.490%	99.680%	98.490%	99.678%	97.603%	99.488%
$\pi/2$	98.451%	99.674%	96.859%	98.451%	97.540%	99.479%

TABLE I: Fidelity of the perfect entangling gate U_{ent} for several χ , where $\gamma = \pi/2$. When taking $\chi = 0$, U_{ent} is equivalent to a CZ gate [76]. $\mathcal{F}_{\text{nai}}^{(i)}$ and $\mathcal{F}_{\text{geo}}^{(i)}$ imply the fidelity for the naive dynamical and geometric gates for the i th block, respectively. \mathcal{F}_{nai} and \mathcal{F}_{geo} are the overall fidelities.

der the ones for the naive dynamical gates. This indicates the geometric gates in each block have higher fidelity compared to the naive gates. With the fidelity in each block in mind, we can further calculate the fidelity for the entire evolution matrix. The specific expression is derived in Appendix C, where

$$\mathcal{F} = \frac{1}{5} + \frac{1}{5}(\mathcal{F}^{(1)} + \mathcal{F}^{(2)})^2. \quad (32)$$

In Table I, we show the fidelity for several values of χ . For all the cases, the fidelities related to the geometric gates are surpassing their dynamical counterparts. Considering the region of $-\pi/2 \leq \chi \leq \pi/2$, the fidelity for the geometric gates can surpass 99%. Specifically, when taking $\chi = -\pi/2$, the fidelity of geometric gate is with its largest value of 99.508%.

V. CONCLUSION

In conclusion, we have proposed a framework to realize non-adiabatic geometric gates for ST qubits in semiconductor quantum dot. By only modulating the time-dependent exchange interaction between neighboring quantum dot, both single- and two-qubit geometric gates can be implemented without introducing an extra microwave field. The results clearly show that the achieved geometric gate is not only superior to its counterpart, namely the naive dynamical gate, with a high fidelity surpassing 99%, but can also realize high-speed gate operation with a gating time of nanosecond. Our result indicates the superiority of the geometric gate, which has great potential to implement robust quantum computing.

ACKNOWLEDGMENTS

This work was supported by the National Natural Science Foundation of China (Grant No. 11905065, 11874156), and the Science and Technology Program of Guangzhou (Grant No. 2019050001).

Appendix A: Filter function

To calculate the filter function, one need to use a control matrix $\mathbf{R}(t) \equiv (\mathbf{R}_x(t), \mathbf{R}_y(t), \mathbf{R}_z(t))^T$ with $\mathbf{R}_j(t) \equiv$

$(R_{jx}(t), R_{jy}(t), R_{jz}(t))$ [59], each component of which has the form as

$$R_{jk}(t) \equiv [\mathbf{R}(t)]_{jk} = \frac{\text{Tr}[U_c^\dagger(t)\sigma_j U_c(t)\sigma_k]}{2}, \quad (A1)$$

where $j, k \in \{x, y, z\}$. Here, the evolution operator $U_c(t)$ is the solution to the noise-free Schrodinger equation $i\frac{\partial U_c(t)}{\partial t} = H_c(t)U_c(t)$, with H_c denoting the noise-free Hamiltonian. For our case, the defined control matrix is slightly different to the original one. This is owing to the fact that the charge noise enters the Hamiltonian via $\delta J(t) = g[J(t)]\delta\epsilon(t)$, where the fluctuation $\delta\epsilon(t)$ rather than $J(t)$ exhibits the $1/f$ -type noise spectrum. Therefore, we consider

$$R_{jk}(t) = g[J(t)] \frac{\text{Tr}[U_c^\dagger(t)\sigma_j U_c(t)\sigma_k]}{2}. \quad (A2)$$

On the other hand, the Fourier transform of the control matrix in the frequency domain is

$$R_{jk}(\omega) = -i\omega \int_0^T dt R_{jk}(t) e^{i\omega t}. \quad (A3)$$

For a given noise power spectral density $S_{ij}(\omega)$, the average fidelity is therefore [59]

$$\mathcal{F}_{\text{av}} \simeq 1 - \frac{1}{2\pi} \sum_{i,j,k=x,y,z} \int_{-\infty}^{\infty} \frac{d\omega}{\omega^2} S_{ij}(\omega) R_{jk}(\omega) R_{ik}^*(\omega). \quad (A4)$$

Then, we show how to calculate the filter function for the geometric gate, which is designed using the piecewise Hamiltonian (see Eq. 6). For the piecewise Hamiltonian, define the evolution operator during each interval as

$$U_l(t) = e^{-iH_l(t-t_{l-1})}. \quad (A5)$$

Further, define the corresponding piecewise control matrix in each interval as

$$R_{jk}^{(l)}(t) = [\mathbf{R}^{(l)}(t)]_{jk} = J(t_l) \frac{\text{Tr}[U_l^\dagger(t)\sigma_j U_l(t)\sigma_k]}{2}, \quad (A6)$$

and thus, we have

$$R_{jk}^{(l)}(\omega) = [\mathbf{R}^{(l)}(\omega)]_{jk} = -i\omega \int_0^{t_l-t_{l-1}} dt R_{jk}^{(l)}(t) e^{i\omega t}. \quad (A7)$$

According to Ref. [59], the whole control matrix in the frequency domain is

$$R_{jk}(\omega) = [\mathbf{R}(\omega)]_{jk} = \sum_{l=1}^n e^{i\omega t_{l-1}} R_{ji}^l(\omega) \Lambda_{ik}^{(l-1)}, \quad (A8)$$

where

$$\Lambda_{jk}^{(l)} = [\Lambda^{(l)}]_{jk} = \frac{\text{Tr}[P_l^\dagger(t)\sigma_j P_l(t)\sigma_k]}{2}, \quad (A9)$$

with $P_l = U_l(t_l)U_{l-1}(t_{l-1}), \dots, U_1(t_1)$ and n is the number with respect to the piecewise Hamiltonian. For the single-qubit case, we only consider the charge noise in the σ_z component, in this way, we have

$$\mathcal{F}_{\text{av}} = 1 - \frac{1}{\pi} \int_0^\infty \frac{d\omega}{\omega^2} S(\omega) F_z(\omega). \quad (\text{A10})$$

where the z -component filter function is

$$F_z(\omega) = \sum_{i=x,y,z} R_{zi}(\omega) R_{zi}^*(\omega). \quad (\text{A11})$$

Appendix B: Local invariant

The two-qubit gates can be classified into two types of operations, i.e., the local and non-local transformations. The representative of the two-qubit local gate is the SWAP gate. While one of the most typical non-local gate is the CNOT gate. The CNOT gate can be used to generate the maximally entangled state such that it belongs to the so-called perfect entangling gate [75]. Generally, the condition for a two-qubit gate belonging to the perfect entangling gate is verified by the values of the local invariants, which reads as [75]

$$\sin^2 \chi \leq 4 |G| \leq 1, \quad \text{and} \quad (\text{B1})$$

$$\cos \chi (\cos \chi - G_3) \geq 0.$$

Here, $G = G_1 + iG_2 = |G| e^{i\chi}$, and

$$\begin{aligned} G_1 &= \text{Re} \left[\frac{\text{Tr}^2[m(U)]}{16} \right], \\ G_2 &= \text{Im} \left[\frac{\text{Tr}^2[m(U)]}{16} \right], \\ G_3 &= \frac{\text{Tr}^2[m(U)] - \text{Tr}[m^2(U)]}{4}. \end{aligned} \quad (\text{B2})$$

are termed as the local invariants. Specifically, the unitary and symmetric matrix $m(U)$ depends on the given operator U : $m(U) = (Q^\dagger U Q)^T Q^\dagger U Q$. While Q is the transformation from the standard basic states $\{|00\rangle, |01\rangle, |10\rangle, |11\rangle\}$ to the Bell states $\{|\Phi_1\rangle = 1/\sqrt{2}(|00\rangle + |11\rangle), |\Phi_2\rangle = i/\sqrt{2}(|01\rangle + |10\rangle), |\Phi_3\rangle = 1/\sqrt{2}(|01\rangle - |10\rangle), |\Phi_4\rangle = i/\sqrt{2}(|00\rangle - |11\rangle)\}$ [77], such that

$$Q = \frac{1}{\sqrt{2}} \begin{pmatrix} 1 & 0 & 0 & i \\ 0 & i & 1 & 0 \\ 0 & i & -1 & 0 \\ 1 & 0 & 0 & -i \end{pmatrix}. \quad (\text{B3})$$

Appendix C: Two-qubit fidelity

The fidelity of the two-qubit gate can be calculated using the formula [78]

$$\mathcal{F} = \frac{\text{Tr}(UU^\dagger) + (|\text{Tr}(U_{\text{ideal}}^\dagger U)|)^2}{d(d+1)}. \quad (\text{C1})$$

Here, U_{ideal} denotes the ideal target gate operation, U is the actual unitary operation, and d represents the dimension of the Hilbert space. Since the two-qubit Hamiltonian in Eq. (22) is block diagonalized, the corresponding operator U_{ideal} can be expressed as

$$U_{\text{ideal}}^\dagger = \begin{pmatrix} a_{11} & a_{12} & 0 & 0 \\ a_{21} & a_{22} & 0 & 0 \\ 0 & 0 & a_{33} & a_{34} \\ 0 & 0 & a_{43} & a_{44} \end{pmatrix}, \quad (\text{C2})$$

and U can be written as

$$U = \begin{pmatrix} b_{11} & b_{12} & 0 & 0 \\ b_{21} & b_{22} & 0 & 0 \\ 0 & 0 & b_{33} & b_{34} \\ 0 & 0 & b_{43} & b_{44} \end{pmatrix}. \quad (\text{C3})$$

We further define

$$U_{i1}^\dagger = \begin{pmatrix} a_{11} & a_{12} \\ a_{21} & a_{22} \end{pmatrix}, \quad U_{i2}^\dagger = \begin{pmatrix} a_{33} & a_{34} \\ a_{43} & a_{44} \end{pmatrix}, \quad (\text{C4})$$

and

$$U_1 = \begin{pmatrix} b_{11} & b_{12} \\ b_{21} & b_{22} \end{pmatrix}, \quad U_2 = \begin{pmatrix} b_{33} & b_{34} \\ b_{43} & b_{44} \end{pmatrix}. \quad (\text{C5})$$

Further, we calculate the term of $\text{Tr}(U_{\text{ideal}}^\dagger U)$:

$$\begin{aligned} \text{Tr}(U_{\text{ideal}}^\dagger U) &= a_{11}b_{11} + a_{12}b_{21} + a_{21}b_{12} + a_{22}b_{22} \\ &\quad + a_{33}b_{33} + a_{34}b_{43} + a_{43}b_{34} + a_{43}b_{44}. \end{aligned} \quad (\text{C6})$$

On the other hand, because the matrix for the operator is diagonalized, each block can be treated as a pseudo single-qubit gate. In this way, the fidelity with respect to each block can also be calculated as

$$\begin{aligned} \mathcal{F}^{(1)} &= \frac{\text{Tr}(U_{i1}^\dagger U_1)}{2} \\ &= \frac{a_{11}b_{11} + a_{12}b_{21} + a_{21}b_{12} + a_{22}b_{22}}{2}, \\ \mathcal{F}^{(2)} &= \frac{\text{Tr}(U_{i2}^\dagger U_2)}{2} \\ &= \frac{a_{33}b_{33} + a_{34}b_{43} + a_{43}b_{34} + a_{43}b_{44}}{2}. \end{aligned} \quad (\text{C7})$$

By inserting Eq. (C7) and Eq. (C6) into Eq. (C1), we can get

$$\mathcal{F} = \frac{4 + (|\text{Tr}(U_{i1}^\dagger U_1) + \text{Tr}(U_{i2}^\dagger U_2)|)^2}{4 \times 5} = \frac{1}{5} + \frac{(\mathcal{F}^{(1)} + \mathcal{F}^{(2)})^2}{5}, \quad (\text{C8})$$

where, we have used $UU^\dagger = \hat{I}$, while \hat{I} is the identity operator and $\text{Tr}(UU^\dagger) = 4$ with $d = 4$.

[1] A. Chatterjee, P. Stevenson, S. De Franceschi, A. Morello, N. P. de Leon, and F. Kuemmeth, *Nat. Rev. Phys.* **3**, 157 (2021).

[2] D. Loss and D. P. DiVincenzo, *Phys. Rev. A* **57**, 120 (1998).

[3] M. Veldhorst, J. C. C. Hwang, C. H. Yang, A. W. Leenstra, B. de Ronde, J. P. Dehollain, J. T. Muhonen, F. E. Hudson, K. M. Itoh, A. Morello, and A. S. Dzurak, *Nat. Nanotechnol.* **9**, 981 (2014).

[4] W. Huang, C. H. Yang, K. W. Chan, T. Tanttu, B. Hensen, R. C. C. Leon, M. A. Fogarty, J. C. C. Hwang, F. E. Hudson, K. M. Itoh, A. Morello, A. Laucht, and A. S. Dzurak, *Nature (London)* **569**, 532 (2019).

[5] A. Noiri, K. Takeda, T. Nakajima, T. Kobayashi, A. Sammak, G. Scappucci, and S. Tarucha, (2021), [arXiv:2108.02626](https://arxiv.org/abs/2108.02626).

[6] J. R. Petta, A. C. Johnson, J. M. Taylor, E. A. Laird, A. Yacoby, M. D. Lukin, C. M. Marcus, M. P. Hanson, and A. C. Gossard, *Science* **309**, 2180 (2005).

[7] S. Foletti, H. Bluhm, D. Mahalu, V. Umansky, and A. Yacoby, *Nat. Phys.* **5**, 903 (2009).

[8] C. Zhang, R. E. Throckmorton, X.-C. Yang, X. Wang, E. Barnes, and S. Das Sarma, *Phys. Rev. Lett.* **118**, 216802 (2017).

[9] K. Takeda, A. Noiri, J. Yoneda, T. Nakajima, and S. Tarucha, *Phys. Rev. Lett.* **124**, 117701 (2020).

[10] P. Cerfontaine, T. Botzem, J. Ritzmann, S. S. Humpohl, A. Ludwig, D. Schuh, D. Bougeard, A. D. Wieck, and H. Bluhm, *Nat. Commun.* **11**, 4144 (2020).

[11] F. Fedele, A. Chatterjee, S. Fallahi, G. C. Gardner, M. J. Manfra, and F. Kuemmeth, (2021), [arXiv:2105.01392](https://arxiv.org/abs/2105.01392).

[12] Z. Shi, C. B. Simmons, J. R. Prance, J. K. Gamble, T. S. Koh, Y.-P. Shim, X. Hu, D. E. Savage, M. G. Lagally, M. A. Eriksson, M. Friesen, and S. N. Coppersmith, *Phys. Rev. Lett.* **108**, 140503 (2012).

[13] A. Frees, S. Mehl, J. K. Gamble, M. Friesen, and S. N. Coppersmith, *npj Quantum Inf.* **5**, 73 (2019).

[14] D. P. DiVincenzo, D. Bacon, J. Kempe, G. Burkard, and K. B. Whaley, *Nature (London)* **408**, 339 (2000).

[15] E. A. Laird, J. M. Taylor, D. P. DiVincenzo, C. M. Marcus, M. P. Hanson, and A. C. Gossard, *Phys. Rev. B* **82**, 075403 (2010).

[16] J. M. Taylor, V. Srinivasa, and J. Medford, *Phys. Rev. Lett.* **111**, 050502 (2013).

[17] J. Medford, J. Beil, J. M. Taylor, E. I. Rashba, H. Lu, A. C. Gossard, and C. M. Marcus, *Phys. Rev. Lett.* **111**, 050501 (2013).

[18] V. N. Ciriano-Tejel, M. A. Fogarty, S. Schaal, L. Huitin, B. Bertrand, L. Ibberson, M. F. Gonzalez-Zalba, J. Li, Y.-M. Niquet, M. Vinet, and J. J. Morton, *PRX Quantum* **2**, 010353 (2021).

[19] A. Bermeister, D. Keith, and D. Culcer, *Appl. Phys. Lett.* **105**, 192102 (2014).

[20] K. W. Chan, W. Huang, C. H. Yang, J. C. C. Hwang, B. Hensen, T. Tanttu, F. E. Hudson, K. M. Itoh, A. Laucht, A. Morello, and A. S. Dzurak, *Phys. Rev. Appl.* **10**, 044017 (2018).

[21] F. Martins, F. K. Malinowski, P. D. Nissen, E. Barnes, S. Fallahi, G. C. Gardner, M. J. Manfra, C. M. Marcus, and F. Kuemmeth, *Phys. Rev. Lett.* **116**, 116801 (2016).

[22] X. Wang, L. S. Bishop, E. Barnes, J. P. Kestner, and S. D. Sarma, *Phys. Rev. A* **89**, 022310 (2014).

[23] R. E. Throckmorton, C. Zhang, X.-C. Yang, X. Wang, E. Barnes, and S. Das Sarma, *Phys. Rev. B* **96**, 195424 (2017).

[24] M. V. Berry, *Proc. Roy. Soc. A.* **392**, 45 (1984).

[25] J. Pachos, P. Zanardi, and M. Rasetti, *Phys. Rev. A* **61**, 010305 (1999).

[26] P. Zanardi and M. Rasetti, *Phys. Lett. A* **264**, 94 (1999).

[27] L.-M. Duan, J. I. Cirac, and P. Zoller, *Science* **292**, 1695 (2001).

[28] S.-L. Zhu and Z. D. Wang, *Phys. Rev. Lett.* **89**, 097902 (2002).

[29] S.-L. Zhu and Z. D. Wang, *Phys. Rev. Lett.* **91**, 187902 (2003).

[30] Y. Aharonov and J. Anandan, *Phys. Rev. Lett.* **58**, 1593 (1987).

[31] A. A. Abdumalikov Jr, J. M. Fink, K. Juliusson, M. Pechal, S. Berger, A. Wallraff, and S. Filipp, *Nature (London)* **496**, 482 (2013).

[32] Y. Xu, W. Cai, Y. Ma, X. Mu, L. Hu, T. Chen, H. Wang, Y. P. Song, Z.-Y. Xue, Z.-q. Yin, and L. Sun, *Phys. Rev. Lett.* **121**, 110501 (2018).

[33] T. Chen and Z.-Y. Xue, *Phys. Rev. Appl.* **10**, 054051 (2018).

[34] B.-J. Liu, X.-K. Song, Z.-Y. Xue, X. Wang, and M.-H. Yung, *Phys. Rev. Lett.* **123**, 100501 (2019).

[35] D. J. Egger, M. Ganzhorn, G. Salis, A. Fuhrer, P. Mueller, P. K. Barkoutsos, N. Moll, I. Tavernelli, and S. Filipp, *Phys. Rev. Appl.* **11**, 014017 (2019).

[36] Y. Xu, Z. Hua, T. Chen, X. Pan, X. Li, J. Han, W. Cai, Y. Ma, H. Wang, Y. P. Song, Z.-Y. Xue, and L. Sun, *Phys. Rev. Lett.* **124**, 230503 (2020).

[37] J. Xu, S. Li, T. Chen, and Z.-Y. Xue, *Front. Phys.* **15**, 41503 (2020).

[38] T. Chen and Z.-Y. Xue, *Phys. Rev. Appl.* **14**, 064009 (2020).

[39] S. Li, J. Xue, T. Chen, and Z.-Y. Xue, *Adv. Quantum Technol.* **4**, 2000140 (2021).

[40] C.-Y. Ding, L.-N. Ji, T. Chen, and Z.-Y. Xue, *Quantum Sci. Technol.* (2021).

[41] C.-Y. Ding, Y. Liang, K.-Z. Yu, and Z.-Y. Xue, *Appl. Phys. Lett.* **119**, 184001 (2021).

[42] M.-Z. Ai, S. Li, Z. Hou, R. He, Z.-H. Qian, Z.-Y. Xue, J.-M. Cui, Y.-F. Huang, C.-F. Li, and G.-C. Guo, *Phys. Rev. Appl.* **14**, 054062 (2020).

[43] M.-Z. Ai, S. Li, R. He, Z.-Y. Xue, J.-M. Cui, Y.-F. Huang, C.-F. Li, and G.-C. Guo, (2021), [arXiv:2101.07483](https://arxiv.org/abs/2101.07483).

[44] A.-L. Guo, T. Tu, L.-T. Zhu, and C.-F. Li, *Phys. Rev. Lett.* **38**, 094203 (2021).

[45] P. Solinas, P. Zanardi, N. Zanghì, and F. Rossi, *Phys. Rev. A* **67**, 052309 (2003).

[46] V. A. Mousolou, C. M. Canali, and E. Sjöqvist, *New J. Phys.* **16**, 013029 (2014).

[47] V. Azimi Mousolou, *Phys. Rev. A* **96**, 012307 (2017).

[48] C. Zhang, T. Chen, S. Li, X. Wang, and Z.-Y. Xue, *Phys. Rev. A* **101**, 052302 (2020).

[49] P. Z. Zhao, X.-D. Cui, G. F. Xu, E. Sjöqvist, and D. M. Tong, *Phys. Rev. A* **96**, 052316 (2017).

[50] K. Takeda, A. Noiri, J. Yoneda, T. Nakajima, and S. Tarucha, *Phys. Rev. Lett.* **124**, 117701 (2020).

[51] J. Yoneda, K. Takeda, T. Otsuka, T. Nakajima, M. R. Delbecq, G. Allison, T. Honda, T. Kodera, S. Oda, Y. Hoshi, N. Usami,

K. M. Itoh, and S. Tarucha, *Nat. Nanotechnol.* **13**, 102 (2018).

[52] S. Shevchenko, S. Ashhab, and F. Nori, *Phys. Rep.* **492**, 1 (2010).

[53] J. Stehlik, Y. Dovzhenko, J. R. Petta, J. R. Johansson, F. Nori, H. Lu, and A. C. Gossard, *Phys. Rev. B* **86**, 121303 (2012).

[54] L. Wang, T. Tu, B. Gong, C. Zhou, and G.-C. Guo, *Sci. Rep.* **6**, 19048 (2016).

[55] J. Emerson, R. Alicki, and K. Życzkowski, *J. OPT. B-QUANTUM S O* **7**, S347 (2005).

[56] E. Knill, D. Leibfried, R. Reichle, J. Britton, R. B. Blakestad, J. D. Jost, C. Langer, R. Ozeri, S. Seidelin, and D. J. Wineland, *Phys. Rev. A* **77**, 012307 (2008).

[57] E. Magesan, J. M. Gambetta, B. R. Johnson, C. A. Ryan, J. M. Chow, S. T. Merkel, M. P. da Silva, G. A. Keefe, M. B. Rothwell, T. A. Ohki, M. B. Ketchen, and M. Steffen, *Phys. Rev. Lett.* **109**, 080505 (2012).

[58] T. Green, H. Uys, and M. J. Biercuk, *Phys. Rev. Lett.* **109**, 020501 (2012).

[59] T. J. Green, J. Sastrawan, H. Uys, and M. J. Biercuk, *New J. Phys.* **15**, 095004 (2013).

[60] G. A. Paz-Silva and L. Viola, *Phys. Rev. Lett.* **113**, 250501 (2014).

[61] D. Buterakos, S. Das Sarma, and E. Barnes, *PRX Quantum* **2**, 010341 (2021).

[62] M. C. Collodo, J. Herrmann, N. Lacroix, C. K. Andersen, A. Remm, S. Lazar, J.-C. Besse, T. Walter, A. Wallraff, and C. Eichler, *Phys. Rev. Lett.* **125**, 240502 (2020).

[63] G. Shinkai, T. Hayashi, T. Ota, and T. Fujisawa, *Phys. Rev. Lett.* **103**, 056802 (2009).

[64] J. M. Nichol, L. A. Orona, S. P. Harvey, S. Fallahi, G. C. Gardner, M. J. Manfra, and A. Yacoby, *npj Quantum Inf.* **3**, 3 (2017).

[65] M. A. Nielsen and I. Chuang, “Quantum computation and quantum information,” (2002).

[66] J. Klinovaja, D. Stepanenko, B. I. Halperin, and D. Loss, *Phys. Rev. B* **86**, 085423 (2012).

[67] R. M. Jock, N. T. Jacobson, M. Rudolph, D. R. Ward, and D. R. Luhman, (2021), [arXiv:2102.12068](https://arxiv.org/abs/2102.12068).

[68] E. Sjöqvist, *Int. J. Quantum Chem.* **115**, 1311 (2015).

[69] X.-C. Yang and X. Wang, *Sci. Rep.* **6**, 28996 (2016).

[70] E. Barnes, M. S. Rudner, F. Martins, F. K. Malinowski, C. M. Marcus, and F. Kuemmeth, *Phys. Rev. B* **93**, 121407 (2016).

[71] T. Struck, A. Hollmann, F. Schauer, O. Fedorets, and L. R. Schreiber, *npj Quantum Inf.* **6**, 40 (2020).

[72] E. Barnes, F. A. Calderon-Vargas, W. Dong, B. Li, J. Zeng, and F. Zhuang, (2021), [arXiv:2103.16015](https://arxiv.org/abs/2103.16015).

[73] L. M. K. Vandersypen and I. L. Chuang, *Rev. Mod. Phys.* **76**, 1037 (2005).

[74] R. Li, X. Hu, and J. Q. You, *Phys. Rev. B* **86**, 205306 (2012).

[75] F. A. Calderon-Vargas and J. P. Kestner, *Phys. Rev. B* **91**, 035301 (2015).

[76] T. F. Watson, S. G. J. Philips, E. Kawakami, D. R. Ward, P. Scalino, M. Veldhorst, D. E. Savage, M. G. Lagally, M. Friesen, S. N. Coppersmith, M. A. Eriksson, and L. M. K. Vandersypen, *Nature (London)* **555**, 633 (2018).

[77] Y. Makhlin, *Quantum Inf. Proc.* **1**, 243 (2002).

[78] J. Ghosh, S. N. Coppersmith, and M. Friesen, *Phys. Rev. B* **95**, 241307 (2017).